Acta Materialia 213 (2021) 116969

Contents lists available at ScienceDirect

Acta Materialia

journal homepage: www.elsevier.com/locate/actamat

Full length article

Tool-workpiece stick-slip conditions and their effects on torque and heat generation rate in the friction stir welding☆

Xue Wang[a], Yanfei Gao[a,*], Xun Liu[b], Martin McDonnell[c], Zhili Feng[d,*]

[a] Department of Materials Science and Engineering, University of Tennessee, Knoxville, TN 37996, USA
[b] Department of Materials Science and Engineering, Ohio State University, Columbus, OH 43210, USA
[c] US Army Ground Vehicle Systems Center, Warren, MI 48397, USA
[d] Materials Science and Technology Division, Oak Ridge National Laboratory, Oak Ridge, TN 37831, USA

ARTICLE INFO

Article history:
Received 4 October 2020
Revised 2 May 2021
Accepted 3 May 2021
Available online 17 May 2021

Keywords:
Friction stir welding
Interfacial stick-slip condition
Torque
Heat generation rate
Contact analysis and similarity relationship

ABSTRACT

Friction stir welding (FSW) has found increased applications in automotive and aerospace industries due to its advantages of solid-state bonding, no fusion and melting, and versatility in various working conditions and material combinations. However, the relationship among processing parameters, material properties, and bonding extent and fidelity remains largely empirical, primarily because of the lack of the mechanistic understanding of the tool-workpiece frictional behavior that affects our subsequent understanding of microstructural evolution and interface bonding formation. While the tool-workpiece stick-slip condition is believed to dictate the resulting torque and heat generation rate during the welding process, it remains rare and elusive to conduct a quantitative experimental measurement of such interfacial field. On the other hand, numerical simulations based on Computational Fluid Dynamics (CFD) rely on ad hoc assumptions of interfacial pressure and shear-stress conditions, but predictions can only be validated via the medium- and far-range temperature field which is known to be insensitive to the interfacial frictional behavior. This work first presents a comparison among two CFD-based simulation methodologies and the Coupled Eulerian Lagrangian (CEL) model in finite element method, the last of which uses the Coulomb friction so that the stick-slip is naturally developed. Based on the Hill-Bower similarity relationship in the contact analysis, an analytical model is developed here to prove why a constant stick-slip fraction will be developed in the steady state, to correlate the stick-slip fraction to processing parameters such as the tool spin rate, and further to derive dimensionless functions for torque and heat-generation-rate predictions. Pros and cons of various numerical approaches in predicting stick-slip are discussed, and our analytical model has been found to agree well with our numerical simulation and literature experimental results. These analyses provide the critical strain-rate and temperature fields that are needed for the bonding analysis in our future work.

1. Introduction

As firstly invented by The Welding Institute (TWI) of UK in 1991, friction stir welding (FSW) bonds the two workpieces in butt configuration under significant heat generated from tool-workpiece frictional sliding and plastic deformation in the workpieces [1-4]. Because there is no melting involved as opposed to fusion welding, an inherent advantage of the FSW process is its reduced susceptibility of solidification cracking and porosity generation. Furthermore, severe thermomechanical deformation in the weldment zone is capable of refining the material microstructure and resulting into enhanced mechanical properties such as tensile strength and toughness [1,5-8]. As illustrated in Fig. 1, a critical assessment of the FSW process needs to focus on the following three issues:

(1) The tool and workpiece surfaces in contact will certainly not be a full stick mode as this requires an infinite friction. It is commonly accepted that the sliding zone generates heat by frictional process, while additional heating is generated in the entire workpieces by plastic deformation. Consequently, where, how, and to what extent the stick and slip zones are

☆ This manuscript has been co-authored by UT-Battelle, LLC, under contract DE-AC05-00OR22725 with the US Department of Energy (DOE). The US government retains and the publisher, by accepting the article for publication, acknowledges that the US government retains a nonexclusive, paid-up, irrevocable, worldwide license to publish or reproduce the published form of this manuscript, or allow others to do so, for US government purposes. DOE will provide public access to these results of federally sponsored research in accordance with the DOE Public Access Plan (http://energy.gov/downloads/doe-public-access-plan)

* Corresponding authors.
E-mail addresses: ygao7@utk.edu (Y. Gao), fengz@ornl.gov (Z. Feng).

https://doi.org/10.1016/j.actamat.2021.116969
1359-6454/

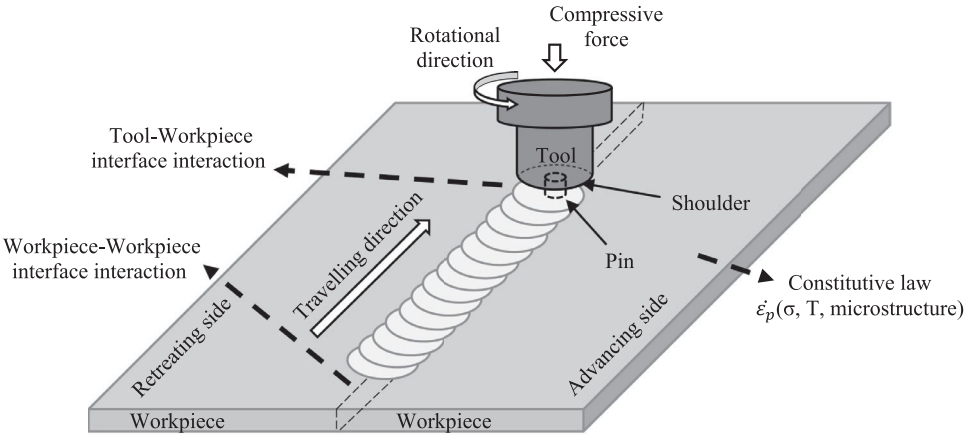

Fig. 1. Schematic illustration of the friction stir welding (FSW) process.

developed will dictate the heat generate rate, material flow, and mechanical responses such as the torque applied on the tool. This is the focus of this paper.

(2) A lot of important outcomes rely on a good understanding of the interface frictional conditions. Microstructural evolution and the resulting property modifications in the thermomechanically affected zone (TMAZ) and the heat affected zone (HAZ) are certainly governed by the material flow fields. The extent and quality of the solid-state bonding between workpieces in friction stir welding has been routinely studied from an experimental point of view, as the relevant modeling development falls behind. Solid-state bonding models can be summarized as primarily inter-diffusional bonding and asperity crushing model, as reviewed by Cai et al. [9]. Our previous work in [10] suggests the critical importance of triaxial creep deformation in driving the closure of interfacial cavities, which certainly relies on an accurate modeling of material flow fields under FSW. Resolving the contradictions in [9] and [10] requires inputs of the strain-rate and temperature fields, both of which rely on the stick-slip analysis. Results from this paper thus provide the foundation for the bonding model in our future work.

(3) Any quantitative numerical prediction needs well calibrated constitutive models for the workpiece material, of which the difficulties lie on the microstructural evolution associated with the severe plastic deformation. This issue will not be elaborated here, and we restrict our studies to the hyperbolic-sine creep law and the Johnson-Cook model.

Since the FSW involves highly coupled thermomechanical processes, only medium- and far-range temperature and deformation fields can be routinely measured, but short-range stick-slip properties underneath the tool are not easily amenable to experimental investigations. Clearly, numerical simulations have advantages in evaluating frictional behavior, contact condition, material flow patterns, and others during such severe thermomechanical processes. The most widely used approach is computational fluid dynamics (CFD), in which workpieces are oftentimes modeled as non-Newtonian fluids and their elastic response is neglected. For example, Seidel and Reynolds [11] adopted two-dimensional (2D) CFD to investigate the material flow around the tool. Ulysse [12] conducted three-dimensional (3D) simulations using a commercial CFD software, FIDAP, and studied the effect of tool speeds on welding temperature and reaction force. Colegrove and Shercliff [13,14] used FLUENT (another commercial CFD software) to study the temperature distribution and 3D material flow pattern around the tool with complex geometry, whereas the roles of tool rake angle and tool speed in affecting the flow pattern were also investigated. The primary advantage of CFD simulations lies on their superior capability of dealing with complex material flow, which is otherwise difficult to handle by Computational Solid Mechanics (CSM) based simulations. However, one critical issue for these CFD simulations is their ad hoc treatments of contact boundary conditions on the tool-workpiece interface. As will be clear from this work, the interfacial stick-slip condition not only affects the heat generation rate during welding process, but also dictates the material flow and the subsequent bonding formation and evolution. It is the full coupling of interfacial frictional stick-slip, material flow, and heat transfer that governs the entire FSW process.

The most widely used analytical model for heat generation was based on Schmidt et al. [15] and Schmidt and Hattel [16], in which a dimensionless parameter δ is introduced to measure the extent of slip. When δ varies from 0 to 1, the interface transitions from fully sticking to fully sliding. Based on these works and numerous follow-up studies, Nandan et al. [3] and Yu et al. [17] concluded that the differential heating rate is given by

$$dq = \left[\delta\mu_f p + (1-\delta)\tau_{yield}\right]\omega r dA, \tag{1}$$

where r is the radius from the tool center, ω is the tool angular velocity (in the unit of radian per second), τ_{yield} is the shear yield strength of the workpiece material, μ_f is the friction coefficient, and p is the normal contact pressure. The common statement in all the above works is that all the heat is generated by friction when δ=1, and at the tool-workpiece contact due to shear plastic deformation when $\delta = 0$. Nandan et al. [3] added another term as the heating from plastic deformation away from the tool-workpiece interface. The former interpretation is problematic, and the latter is incorrect. A detailed explanation of the heat generation rate and the critical issues in boundary conditions (especially p and δ) in CFD simulations will be presented in Section 2. In a high-level perspective paper, Colligan and Mishra [2] summarized a thorough list of independent process variables and dependent process outcomes, and suggested that a mechanistic description of frictional heat generation under FSW conditions is still lacking, and correspondingly a quantitative way of assigning different weighting factors, e.g., in Eq. (1), remains elusive. They emphasized the critical needs of calibrating material and friction parameters in explaining the observed non-monotonic correlations between heat generation and processing conditions, which arises mainly from our poor understanding of the stick-slip condition.

Another difficulty in CFD simulations is the shear-stress interface condition [18-20]. Again, as opposed to CSM based models that can naturally calculate the interfacial stress fields from

Coulomb friction, ad hoc models have to be introduced in CFD. As a step significantly beyond Eq. (1), Chen et al. [19] proposed a novel boundary condition to implement the stick-slip transition at the interface by introducing a critical relative speed, V_C, below which the interface is considered to be in a pseudo-sticking state and the shear stress takes the value of τ_{yield}. In this way, the stick-slip condition was numerically calculated for the first time, which is further validated by microstructural evidences. This novel boundary condition model was also extended to demonstrate successes in capturing the stick-slip transition for the threaded tool/pin [21]. Liu et al. [20] implemented an empirical friction-stress model on tool-workpiece interface to study FSW process for dissimilar materials, which led to improved predictions than simulations based on velocity boundary conditions. However, the development of stick-slip conditions was not reported in this work.

Finite element analysis (FEA) can readily solve the frictional contact problem, but Lagrangian-based FEA cannot handle the severe deformation in FSW. To this end, arbitrary Lagrangian-Eulerian (ALE) formulation in ABAQUS was adopted by Xu et al. [22,23] through re-meshing methodology, which modeled the FSW process as a 2D steady state problem and predicted material flow patterns in good agreement with experimental observations. Schmidt and Hattel [24] developed a 3D ALE model through ABAQUS/Explicit and predicted the defect formation during the welding process. But it had reported that ALE method cannot handle excessive mesh distortion and may lead to numerical instability and divergency of numerical solutions in these simulations [25]. Some other works have recently employed the Coupled Eulerian-Lagrangian (CEL) method to simulate the FSW process [26,27]. In this method, the tool is modeled in Lagrangian formulation and the workpiece in Eulerian formulation. Apart from the material flow pattern, the CEL approach is able to predict volumetric defects and mechanical responses during FSW process. In Section 3, we will employ the two ad hoc CFD methodologies as discussed in the preceding paragraph [19,20] as benchmarks to compare to our CEL simulation results in Section 4, with the focus on comparing the predicted interfacial stick-slip ratios from these different frictional boundary conditions.

In a number of seminal works by Shercliff and co-authors [28-30], the material flow fields under friction stir spot welding were visualized by using two types of aluminum alloys with similar strengths, but their copper content different made them distinct upon etching. This procedure and the resulting flow visualization motivated them to develop a flow pattern that is largely kinematically determined, with the stick condition inside the contact and an annular zone of the slip condition at the contact periphery. In their subsequent numerical simulations, Jedrasiak and Shercliff [29,30] applied a physically based kinematic boundary condition on the tool-workpiece interface, and thus determined the role of the stick-slip region on our understanding of the heat generation and other processing-outcome relationships. A contact mechanics model, however, has not been developed to prove the existence of a steady-state stick-slip condition, for which the separation of stick and slip zones has a fixed ratio and is independent of time. An analytical interpretation of stick-slip conditions on the tool-workpiece interface, together with their effects on torque and heat generation rate, would be very useful for the FSW applications. This paper aims to tackle this challenge from a contact analysis based on the Hill-Bower similarity relationship, as given in Section 5. This analytical approach can now correlate the steady-state stick-slip ratio to processing parameters, such as tool spinning rate and applied torque. At the meantime, these analytical results provide a platform to validate and verify the CFD and CEL simulation results in Sections 3 and 4; such comparisons based on the stick-slip conditions have not been attempted previously. Additionally, these theoretical predictions can now provide a useful guidance and revisit to experimentally measured data of torque and heat generation rate.

2. Revisiting the heat generation rate

In this Section, we first derive the total heat generation rate from both frictional heating and plastic deformation, and then discuss the limitations of ad hoc boundary conditions oftentimes used in CFD simulations. The following theoretical analysis will pave the foundation for comparing CFD and FEA simulations in Sections 3 and 4.

There are only two sets of field equations in the FSW problem, one being the momentum transfer (or stress balance when inertia force is small) equation in the workpiece, and the other being the bulk energy transport equation, given by

$$\rho C_P\left[\frac{\partial T}{\partial t}+\mathbf{v}\cdot\nabla T\right]=k\nabla^2 T+\alpha_{TQ}\sigma_{ij}\dot{\varepsilon}^p_{ij}, \tag{2}$$

where ρ is the material density, C_P is the heat capacity, T is the temperature, t is time, $\mathbf{v}$ is the material velocity vector, k is the thermal conductivity, σ_{ij} is the stress tensor, $\dot{\varepsilon}^p_{ij}$ is the plastic strain rate, and α_{TQ} is the Taylor-Quinney ratio that measures the fraction of plastic work converted to heat (e.g., 0.6~0.9 for most metals). Latin subscripts run from 1 to 3. Summation convention is implied for repeated indices. The heat generation rate due to plastic deformation is the integral,

$$Q_{plastic}=\alpha_{TQ}\int_{\Omega}\sigma_{ij}\dot{\varepsilon}^p_{ij}dV, \tag{3}$$

over the volume occupied by the two workpieces. Neglecting elastic deformation leads to the approximation of $\int_{\Omega}\sigma_{ij}\dot{\varepsilon}^p_{ij}dV\approx\int_{\Omega}\sigma_{ij}\dot{\varepsilon}_{ij}dV=\int_{\Omega}\sigma_{ij}\dot{u}_{i,j}dV$, where the last step is based on the symmetric nature of stress tensor. Using Gauss theorem, we can convert the bulk integral to a surface one, $\int_{\Omega}\sigma_{ij}\dot{u}_{i,j}dV=\int_{S}\sigma_{ij}\dot{u}_i n_j dA-\int_{\Omega}\sigma_{ij,j}\dot{u}_i dV$, and the last term vanishes due to stress balance equations, $\sigma_{ij,j}=0$. Consequently, the plastic heating rate becomes

$$Q_{plastic}\approx\alpha_{TQ}\int_{S}\sigma_{ij}\dot{u}_i n_j dA\approx\alpha_{TQ}\int_{S}\sigma_{3\theta}\dot{u}_\theta dA \tag{4}$$

where the subscript θ is the polar coordinate on the tool-workpiece interface, and $\dot{u}_\theta=v_\theta$ is the θ-component of the velocity vector in the workpiece. We also note that the frictional heating only occurs in the sliding zone, given by

$$Q_{friction}=\int_{slip}\mu_f p(\omega r-\dot{u}_\theta)dA. \tag{5}$$

Consequently, the total heat generation rate is

$$\begin{aligned}Q_{total}&=Q_{plastic}+Q_{friction}\\&=\alpha_{TQ}\left\{\int_{stick}\tau_{yield}\omega r dA+\int_{slip}\mu_f p\dot{u}_\theta dA\right\}+\int_{slip}\mu_f p(\omega r-\dot{u}_\theta)dA\\&\xrightarrow{\alpha_{TQ}=1}\int_{stick}\tau_{yield}\omega r dA+\int_{slip}\mu_f p\omega r dA\end{aligned} \tag{6}$$

Referring back to Eq. (2) and assuming α_{TQ}=1, it can be clearly seen that all the heat generation due to plastic deformation can be written as a surface integral inside the stick zone, and all the frictional heating as another surface integral inside the slip zone. Adding another bulk integral for plastic heating is thus not needed.

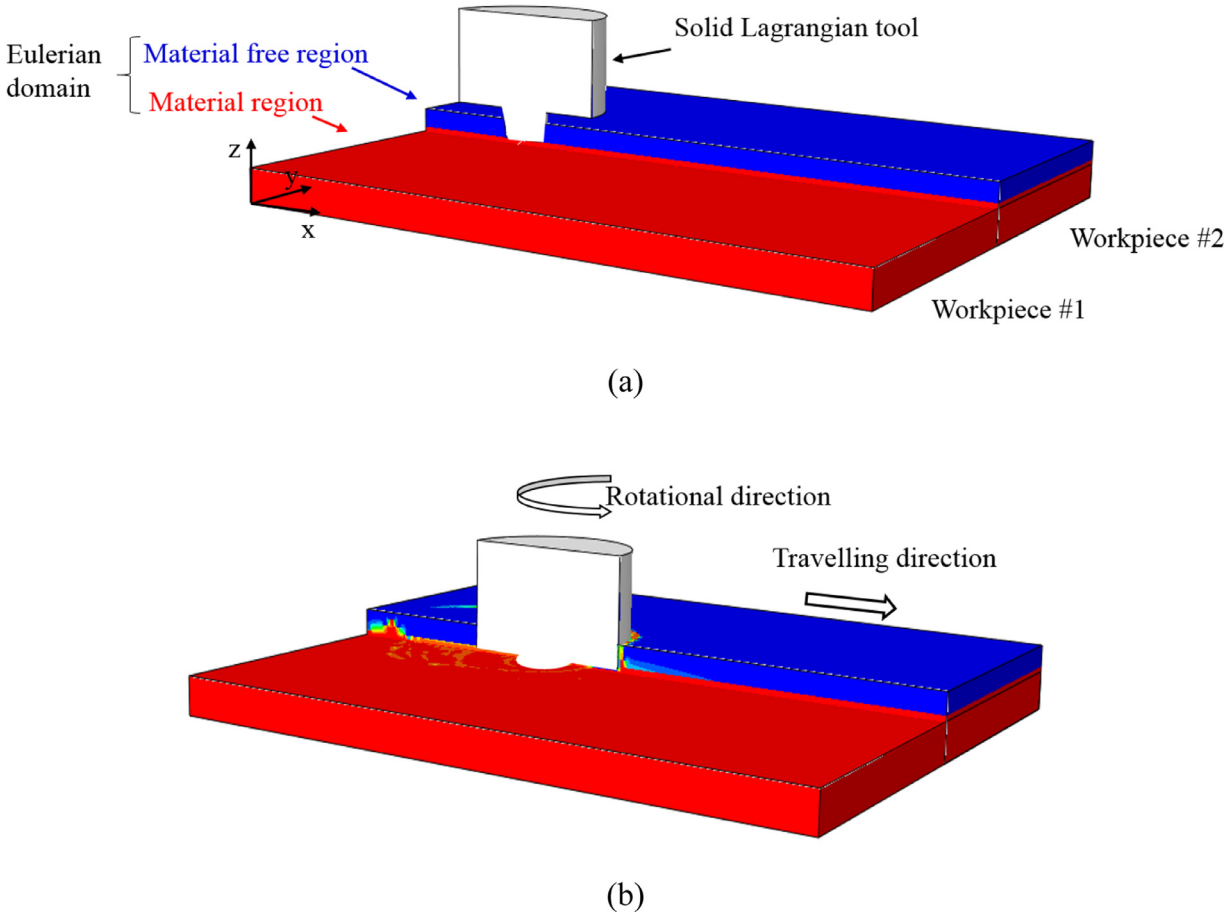

Fig. 2. Problem setup in the Coupled-Eulerian-Lagrangian (CEL) finite element simulation for the FSW process: (a) initial configuration, (b) during the welding process.

Most CFD simulations assume a given contact pressure of p and/or prescribe a value of δ a priori as the boundary/interface condition, instead of computing such pressure and stick-slip distributions as CSM can do for the Coulomb friction. Therefore, some of the CFD simulation results need ad hoc adjustments of p and δ when comparing to experimental measurements such as medium- and far-field temperature distribution [17], while some works predict dubious behavior. For example, a fully stick condition was assumed in Colegrove and Shercliff [31], which clearly over predicted temperature and material deformation zone size. To deal with the stick-slip condition on the tool-workpiece interface, Colegrove and Shercliff, in their later works [32,33], introduced an experimental calibrated contact radius which is smaller than the shoulder radius in their CFD simulation. Therefore, the magnitude and trend of traversing force with difference pin profiles and under various rotational speed were successfully predicted. The contact radius for the shoulder is also defined in numerical simulation models to investigate the heat generation and temperature evolution with respect to tool and plate dimensions and the process parameters in FSW. Atharifar et al. [34] modified the velocity boundary conditions that applied on the tool-workpiece interface to achieve a sliding state, in which the velocity of interface material was assumed to be 65% of the tool velocity. However, they also stated that in order to obtain accurate computational results in various FSW conditions, velocity boundary needs to be adjusted for different welding parameters. Nandan et al. [35] and Arora et al. [36] introduced an empirical parameter to describe the slipping state at tool-workpiece interface with a velocity boundary condition, which again needs to be adjusted to achieve a good agreement of temperature and deformation zone in the weld.

3. Computational Fluid Dynamics (CFD) simulations

Continuum mechanics consists of three sets of equations, including the energy transfer equation in Eq. (2), the kinetic equation (i.e., Navier-Stokes equation for momentum transfer in the Eulerian view, or Navier-Cauchy equation for stress balance in the Lagrangian view), and the material constitutive law. With appropriate boundary and initial conditions, these equations can be solved by finite difference or other methods in CFD, or finite element method in CSM.

3.1. CFD by FLUENT

In CFD simulations, the workpiece can be assumed to be an incompressible non-Newtonian fluid, with the viscosity given by

$$\mu = \frac{\sigma_e}{3\dot{\varepsilon}_e}, \tag{7}$$

where σ_e the Mises effective stress and $\dot{\varepsilon}_e$ is the effective strain rate. The temperature and strain-rate dependent model, as suggested by [37], takes the following form,

$$\sigma_e = \frac{1}{\beta}\ln\left\{\left(\frac{Z}{A}\right)^{1/n} + \left[\left(\frac{Z}{A}\right)^{2/n} + 1\right]^{1/2}\right\}, \tag{8}$$

where A, n, and β are material constants, Z is the Zener-Holloman parameter,

$$Z = \dot{\varepsilon}_e \exp\left(\frac{Q_{def}}{RT}\right), \tag{9}$$

Table 1
Constitutive parameters used in our simulations for AA2024 aluminum alloy [38].

Density (kg/m^3)	A (s^{-1})	n	Q_{def} (kJ/mol)	β (Pa^{-1})
2.7×10^3	2.29×10^{11}	5.46	178	2.09×10^{-8}

R is the gas constant, and Q_{def} is the activation energy. Representative values for these parameters are given in Table 1 for aluminum alloy AA2024 [38].

Our CFD simulations were performed using the commercial software FLUENT, in which two metal sheets occupy the space beneath the tool, with a total dimension of 100 mm × 55 mm × 3mm. The radius of tool shoulder is 6.5 mm, and the radii of the tapered tool pin are 2 mm at the root and 1.75 mm at the tip with a height of 2.4 mm. The entire workpiece space is discretized by 337,620 cells. FLUENT provides a user defined function to implement the viscosity function in Eq. (7), based on the constitutive law in Eq. (8).

Ad hoc boundary conditions have been proposed to describe the friction contact, via the user defined functions in FLUENT. Following [19,39], the interface shear stress is determined from the relative velocity of the tool and workpiece surfaces, i.e., $\mathbf{v}_{rel} = (\omega r - \dot{u}_\theta)\mathbf{e}_\theta$ in Eq. (5) with $\mathbf{e}_\theta$ being the basis vector in θ coordinate. As shown in Fig. 3(a), whether any given location falls into sticking or sliding state depends on comparing the magnitude of this relative speed to a critical value, v_c,

$$\tau_f = \mu_f p \operatorname{sgn}\left(\frac{\mathbf{v}_{rel}}{\|\mathbf{v}_{rel}\|}\right)\begin{cases}1, & \|\mathbf{v}_{rel}\| \geq v_c \\ \tanh\left(\frac{\|\mathbf{v}_{rel}\|}{v_0}\right), & \|\mathbf{v}_{rel}\| < v_c\end{cases} \tag{10}$$

where v_0 is a reference velocity (taken as 0.02 m/s in this work). In contrast to FEA simulations based on the Coulomb friction law, the predicted stick-slip ratio from this model depends on the choice of v_c. Nevertheless, it provides a way to simulate the development of stick-slip in CFD, as opposed to the rather unphysical choice of fixed δ in many other CFD works. To this end, the condition of $\|\mathbf{v}_{rel}\| < v_c$ is denoted as the pseudo-sticking state.

The other type of boundary conditions in FLUENT used in this study follows the work by Liu et al. [20]. Noting that the interfacial shear stress is always limited by the yield strength of the substrate material, the following fitting equation [40] can be used to represent the transient behavior in Fig. 3(b),

$$\tau_f = m\tau_{yield}\left\{1 - \exp\left[-\left(\frac{\mu_f p}{m\tau_{yield}}\right)^{n_f}\right]\right\}^{1/n_f}, \tag{11}$$

where m is called friction factor (taken as 0.95) and n_f is a fitting parameter (taken as 1.7 here). In this model, when $\mu_f p > m\tau_{yield}$, the interfacial shear stress takes the value of τ_{yield} which corresponds to the sticking state.

The above two models have been implemented via user defined functions in FLUENT. In all these CFD simulations, the rotational speed ranges from 600 to 1600 rpm, but the tool traveling speed is kept as 20 mm/min.

3.2. CFD simulation results

Temperature, velocity, strain rate, and flow stress fields are presented in Fig. 4 for CFD simulations with the pseudo-sticking-state model in Fig. 3(a), the empirical friction stress model in Fig. 3(b), and no-slip boundary condition. Four rotational speeds were compared in these simulations. It is noted that different interface conditions give rise to different peak temperature values, and thus clearly different heat generation rates. The interface stick-slip condition can be obtained by inspecting the radial distribution the velocity of workpiece material right underneath the tool shoulder. It

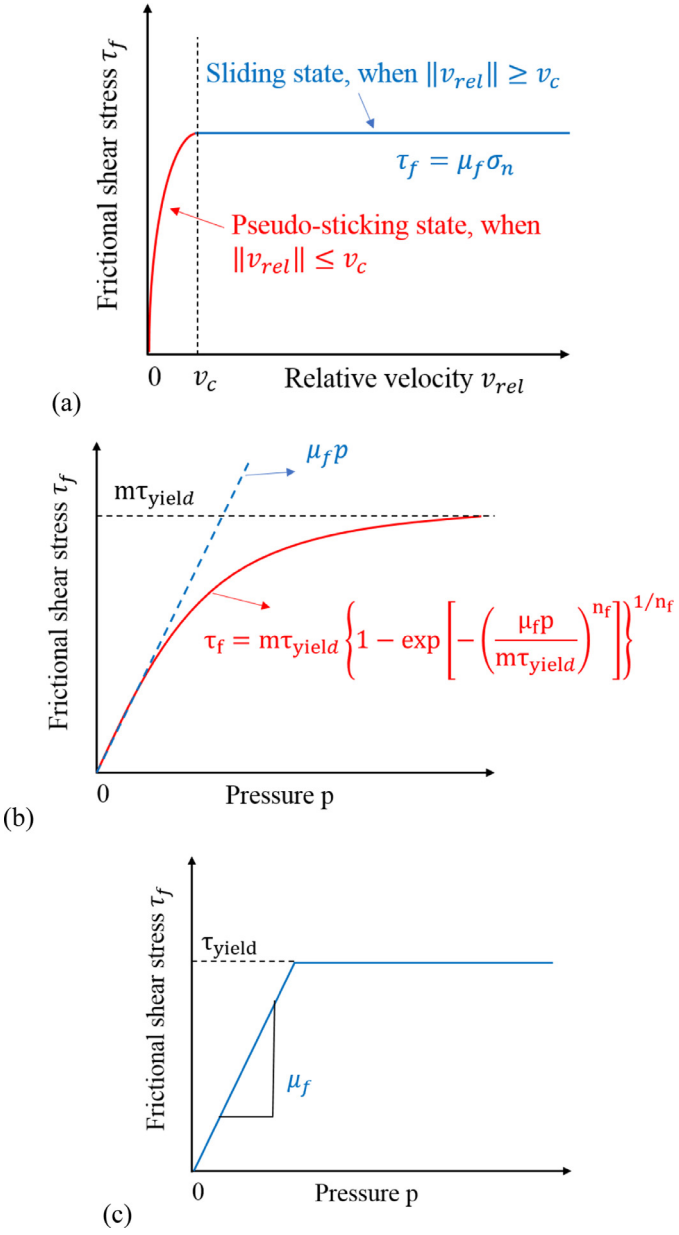

Fig. 3. Three types of friction models: (a) pseudo-sticking-state model in CFD simulations by Chen et al. [19]; (b) empirical frictional boundary condition in CFD simulations by Liu et al. [20]; (c) Coulomb friction used in finite element simulations.

can be seen from the deviation from linearity in Figs. 4(a) and 4(b) that the sticking condition is found in an inner zone (size of c), while an annular sliding zone ($c \leq r \leq a$ as will be illustrated in Fig. 11) exists in which the workpiece velocity lags behind that of the tool. Although both Figs. 4(a) and 4(b) show the same trend of increasing c/a with the increase of ω, the exact stick-slip ratio predicted under the same welding parameters is sensitive to the particular interface condition used in these CFD simulations. The strain rate field, being the velocity gradient, shows similar radial distribution. The flow stress relates to temperature and strain rate from the constitutive law in Eq. (8), so that it is comparably lower underneath the sticking regime than under the sliding regime.

From these results in Fig. 4, several limitations of CFD simulations can now be seen. First, while all the trends with respect to varying ω are the same, different interfacial conditions give different values of stick-slip ratio, which therefore affects the highest temperature and total heat generation rate. Second, axial force and

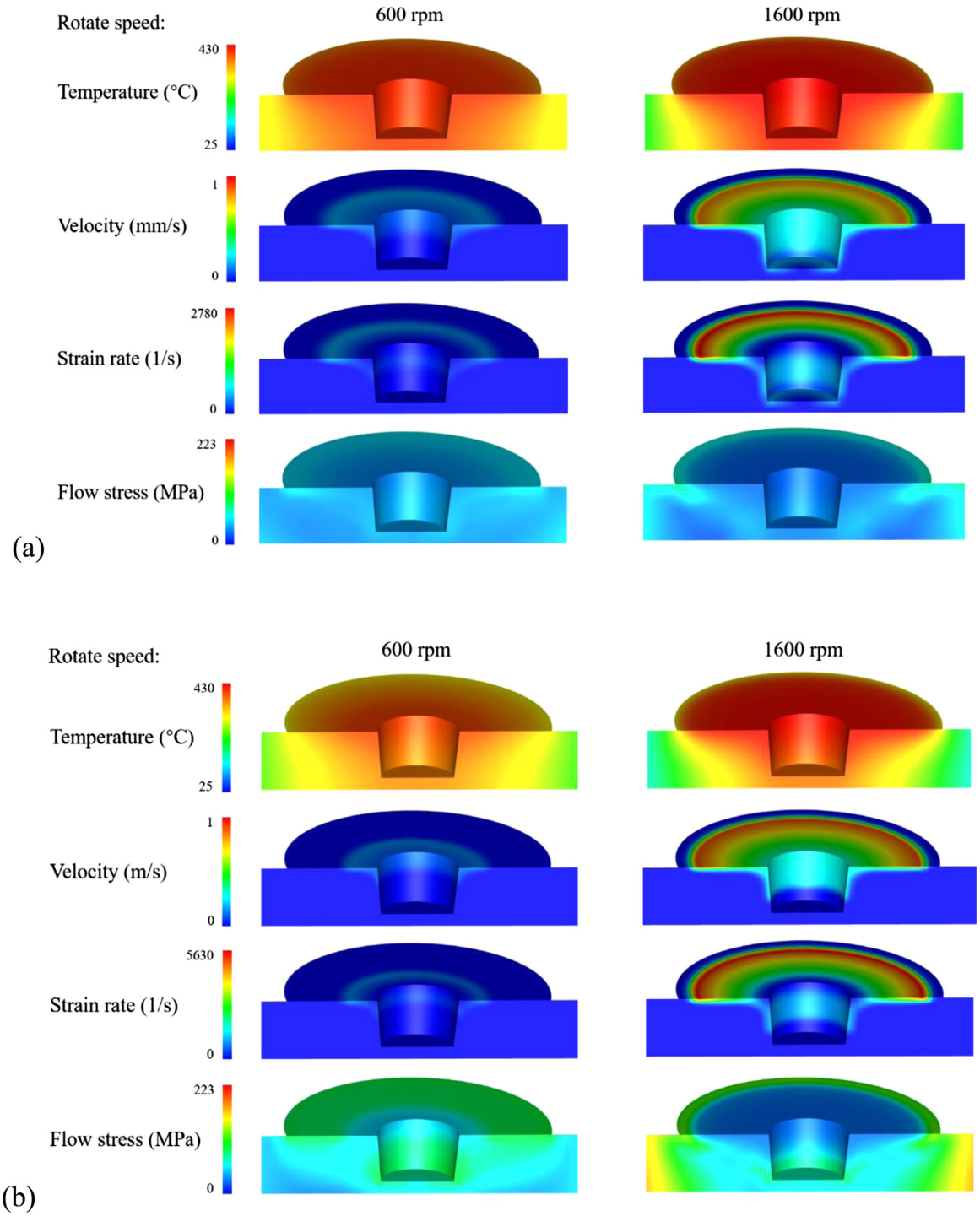

Fig. 4. Temperature, velocity, strain rate, and flow stress fields as predicted by CFD simulations using different frictional boundary conditions: (a) pseudo-sticking-state model in Fig. 3(a); (b) empirical frictional boundary condition in Fig. 3(b).

resulting torque on the tool cannot be directly obtained from CFD simulations; one has to conduct tedious post-processing from the calculated flow stress field. But again, the mechanical responses computed in such a way are problematic as all these CFD simulations in Fig. 4 predict very different thermomechanical fields. Third, when comparing these predictions to experimental measurements that are usually limited to medium- and/or far-range temperature fields, one can arbitrarily change the associated parameters in these ad hoc interface models, such as v_c in Eq. (10), to attain a good agreement, which however reduces the confidence in other predicted fields. Fourth, all results in Fig. 4 are computed from a given pressure (e.g., 50 MPa as adopted here) uniformly distributed on the tool-workpiece interface. As will be shown later in this paper, the actual pressure distribution is nonuniform and has crucial consequences on the resulting stick-slip behavior. All these concerns cast challenges to the development of predictive CFD models for FSW.

The validity of the strong assumption of a constant and uniform pressure distribution can be investigated from an iterative process. As shown in the flowchart in Fig. 5, if the input and computed

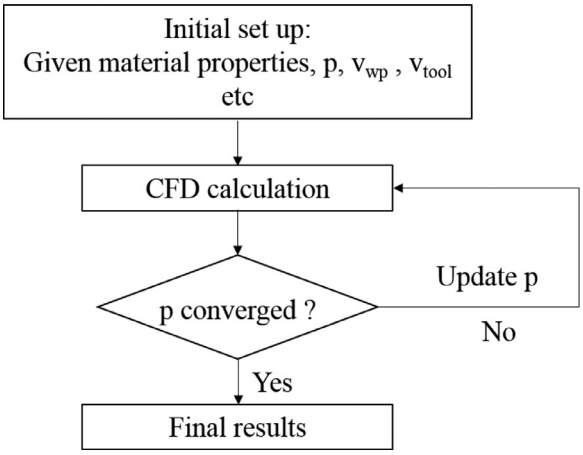

Fig. 5. Flow chart for the pressure iteration process, where p is the pre-specified pressure value in CFD simulations.

pressure are not the same, the computed pressure distribution is then taken as the input for the next round of simulations. This procedure will be repeated until two pressures converge. Applying this iteration to the results in Fig. 4(a), we find out that the area-weighted average pressure converges quickly and decreases from 50 MPa to 39 MPa. As illustrated by the pressure distribution at interface at each iteration in Fig. 6(a), the final computed pressure distribution shows a clear deviation from the initial applied pressure. Except for several points with extremely high values, for most areas, pressure under the tool is far less than 50 MPa and localized between 30-40 MPa during iteration. Results in Fig. 6 are for the pseudo-sticking-state model in Fig. 3(a) and Fig. 4(a) at a given rotational speed. Although changing ω will also change the final converged pressure value and thus iterations are needed for every set of processing and property parameters, the calculations are very tedious and become impractical since it oftentimes takes days for individual simulation job to reach the steady state. The final stick-slip ratio after iteration shows some improvement, but it does not change the fact that this pseudo-sticking-state model in Fig. 3(a) is not a true outcome of frictional contact analysis.

4. Coupled-Eulerian-Lagrangian (CEL) finite element simulations

4.1. CEL by ABAQUS

For CEL finite element simulations, we adopt the Johnson-Cook constitutive law [41], which is a strain, strain rate, and temperature dependent viscoplastic model, given by

$$\sigma_e = \left(A_{JK} + B_{JK}\varepsilon_e^N\right)\left(1 + C_{JK}\ln\frac{\dot{\varepsilon}_e}{\dot{\varepsilon}_0}\right)\left[1 - \left(\frac{T - T_{ref}}{T_{melt} - T_{ref}}\right)^{m_{JK}}\right], \quad (12)$$

where ε_e is the effective strain, $\dot{\varepsilon}_0$ is a characteristic strain rate (taken as 1.0 s^{-1} here), and T_{melt} and T_{ref} are material solidus temperature and reference temperature, respectively. Representative values for the constitutive parameters, A_{JK}, B_{JK}, C_{JK}, N and m_{JK} are given in Table 2 for aluminum alloy AA6061-T6. Density of AA6061-T6 is taken as 2690 kgm^{-3}. A 90% fraction of plastic work

Table 2
Constitutive parameters used in the Johnson-Cook model for AA6061-T6 [26].

A_{JK} (MPa)	B_{JK} (MPa)	C_{JK}	m_{JK}	N	T_{melt} (K)	T_{ref} (K)
324	114	0.002	1.34	0.42	297	856

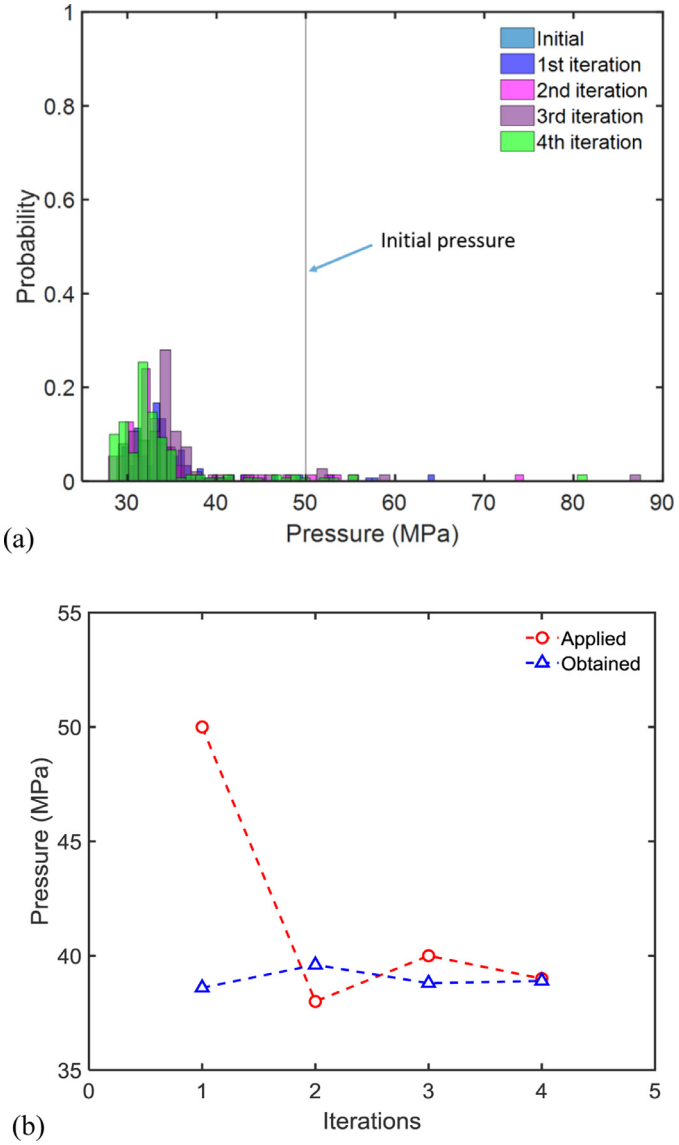

Fig. 6. (a) Probability distribution of the computed pressure value (actually the normal stress of the workpiece at contact). (b) The average pressure at each iteration. These results correspond to the CFD simulation results in Fig. 4(a).

is assumed to be converted to heat, i.e., α_{TQ}=0.9. The relevant thermomechanical properties, including thermal conductivity, specific heat, and elastic constants, are taken from several literature works [26,42-45], as summarized in Table 3. Our work assumes a constant and temperature-independent friction coefficient. Colligan and Mishra [2] have attempted to correlate the temperature dependence of friction coefficient to processing parameters such as rotation speed, while this study appears to suggest that the more relevant dependence should be through the stick-slip ratio.

Conventional finite element simulations are based on the Lagrangian view, so needing to solve the Navier-Cauchy equation for momentum transfer. In CEL simulations using the commercial software ABAQUS, the entire control volume is divided into Eulerian and Lagrangian domains, which helps overcome the difficulty in ad hoc frictional modeling in CFD-based models and the difficulty in large deformation in FEA simulations. As shown in Fig. 2, the tool is modeled as a rigid isothermal Lagrangian body and its movement is controlled by a reference point attached to the bottom surface of the pin. The tool shape and size are the same as in CFD simulations. The entire Eulerian domain is meshed with 128,089

Table 3
Thermomechanical properties for AA6061-T6 [26,45].

Temperature (K)	Specific heat ($Jkg^{-1}K^{-1}$)	Young's modulus (GPa)	Poisson's ratio	Thermal conductivity ($Wm^{-1}K^{-1}$)	Thermal expansion (10^{-6} K^{-1})
298	945	66.94	0.33	162	23.5
373	978	63.21	0.334	177	24.6
422	1000	61.32	0.335	184	25.7
477	1030	56.8	0.336	192	26.6
533	1052	51.15	0.338	201	27.6
589	1080	47.17	0.36	207	28.5
644	1100	43.51	0.4	217	29.6
700	1130	28.77	0.41	229	30.7
755	1276	20.2	0.42	243	-

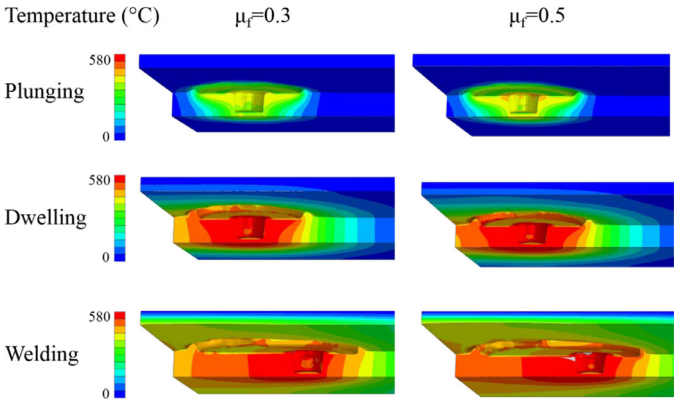

Fig. 7. CEL simulation results showing the temperature fields in workpiece #2 during each FSW stage with three different friction coefficients. Refer to Fig. 2 for model setup.

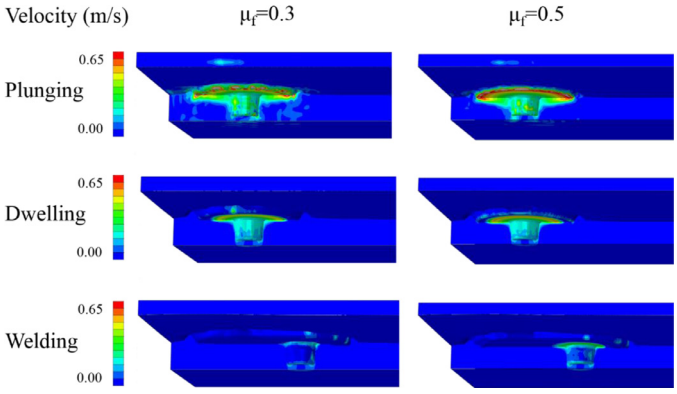

Fig. 8. CEL simulation results showing the velocity field in workpiece #2 during each FSW stage with three different friction coefficients. Refer to Fig. 2 for model setup.

EC3D8RT elements, in which the red part represents two workpieces (each with the dimension of 50 mm × 20 mm × 3mm) and the blue part is empty.

The Lagrangian body is coupled to the Eulerian domain through the contact interaction, using the Coulomb friction law as shown in Fig. 3(c). It should be mentioned that Figs. 3(c) and 3(b) are very different; CFD simulations based on Fig. 3(b) start with a pre-defined pressure, while finite element simulations based on Fig. 3(c) need to determine pressure and stick-slip condition by solving the boundary/initial value problem. In our CEL simulations, three different friction coefficients (μ_f=0.3, 0.5, 0.8) were evaluated to understand its effect on thermomechanical field distributions and stick-slip conditions on tool-workpiece interface. Velocity constraints are applied on side surfaces and bottom surface of the Eulerian domain to avoid material escaping in Fig. 2. The whole simulation process includes three stages: plunging stage (0.2s), dwelling stage (0.2s) and welding stage (2.5s). The tool rotational speed is kept at 1000 rpm, and the welding speed is 3 mm/s.

4.2. CEL simulation results

Simulated temperature and velocity fields in the workpiece #2 during each FSW state with three different friction coefficients are illustrated in Figs. 7 and 8, respectively. Since the view cut is based on a fixed height in the initial configuration, one can actually see some part of workpiece #1 over that original height; these are morphological features not captured in CFD simulations. As these results show, temperature distributions at each stage are very similar in three cases. The highest temperature occurs near the shoulder-pin junction, and a larger friction coefficient will lead to a higher peak temperature. From the velocity contours at different welding stages, one can see that at plunging stage, most of the workpiece material underneath the tool follows the movement of the tool. When reaching to the dwelling stage, material near the outer edge of tool shoulder and pin lags behind, and the size of "sticking" zone shrinks. In comparison, simulations with a higher friction coefficient obtains a larger "sticking" zone size on the interface.

Now switching the view cut along the tool traveling direction in Figs. 7 and 8 (i.e., *xz* plane in Fig. 2) to the lateral cross-sectional direction (i.e., *yz* plane in Fig. 2), we plot the distributions of shear stress, pressure, velocity, and material flow stress for the workpiece materials right underneath the tool shoulder in Figs. 9 and 10. For μ_f=0.5 in Fig. 9, the top row compares several stress measures. While the stick zone can be determined when the shear stress is less than $\mu_f p$, this method turns out to be inaccurate due to the mesh size limitation. Instead, the velocity differences in the bottom row in Fig. 9 shows the inner stick zone and the outer annular sliding zone. The stick zone is the largest at the plunging state, and correspondingly, the shear stress at the tool-workpiece interface is larger than the workpiece flow stress. At the dwelling and welding stages, flow stress underneath the outer edge of shoulder becomes larger than the shear stress at interface, which narrows down in the sticking zone. Velocity distributions for three friction coefficients are compared in Fig. 10, which clearly shows that a higher friction coefficient helps obtain a lager sticking zone.

5. Analytical stick-slip model based on Hill-Bower similarity analysis

Given the same set of processing, geometric, and material constitutive parameters, CFD and CEL simulations in Sections 3 and 4 give very different predictions of thermomechanical responses. While the stick-slip ratio is more trustworthy in Section 4 than in Section 3, these results need to be validated from analytical and experimental results.

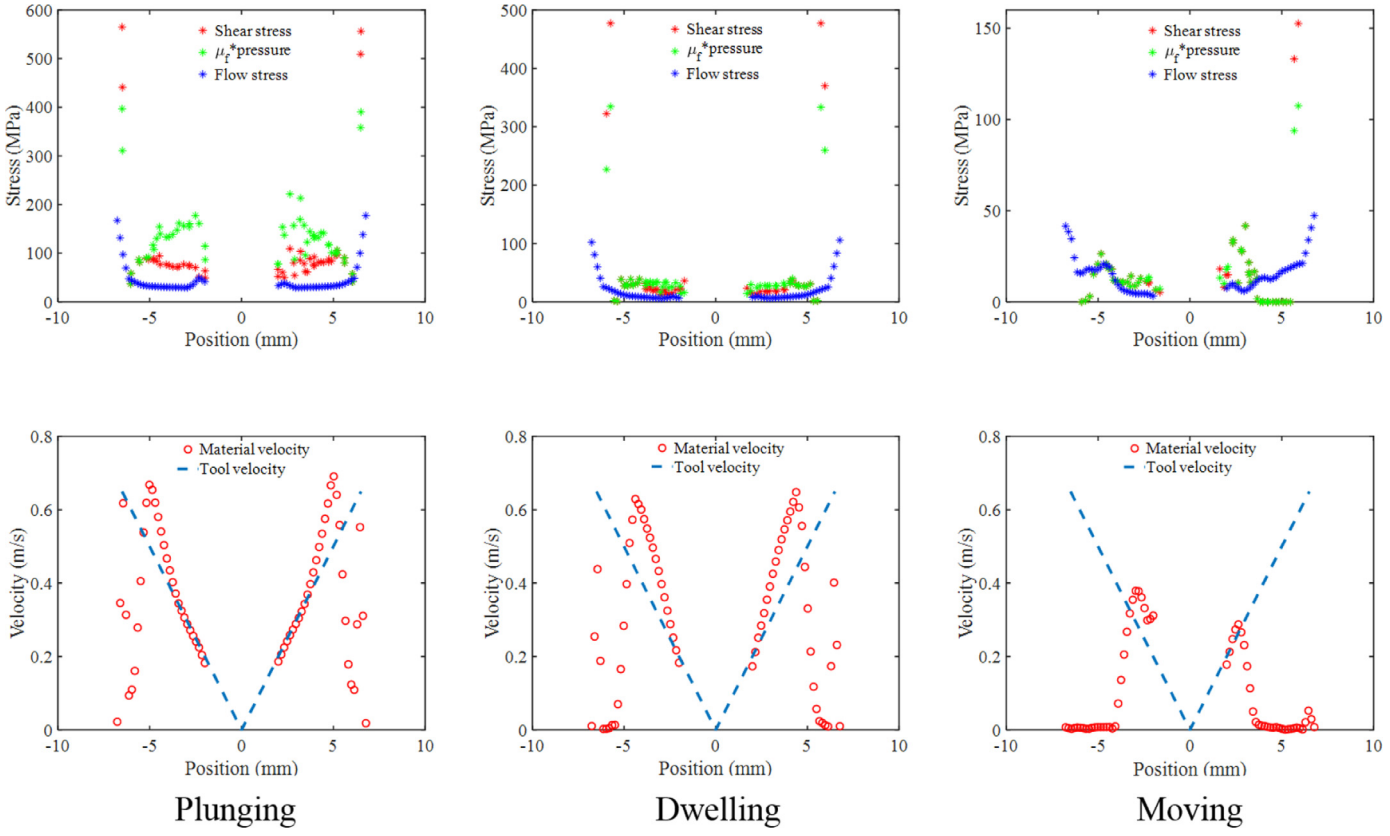

Fig. 9. CEL simulation results showing the material flow stress (top row) and velocity (bottom row) of the workpieces right underneath the tool for μ_f=0.5. Positive location corresponds to the advancing side (workpiece #1), and negative location to the retreating side (workpiece #2).

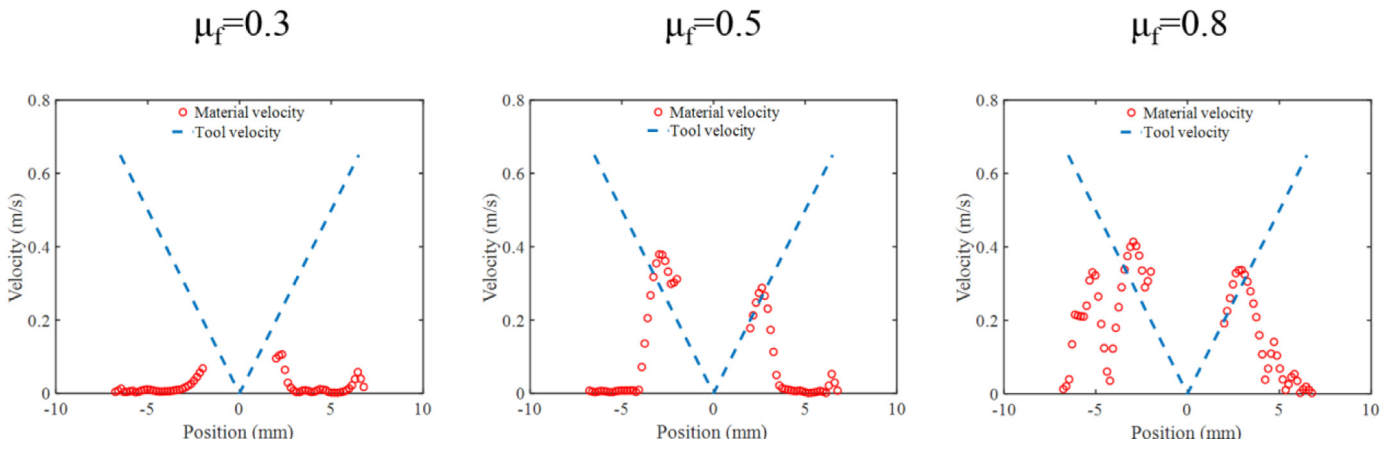

Fig. 10. Steady-state distribution of workpiece velocity right underneath the tool, as calculated from CEL simulations in Fig. 2, for three different friction coefficients.

5.1. Hill-Bower similarity analysis for contact problems

In typical processing conditions, the traveling speed of the tool is much less than ωa, so that only pure torsion needs to be analyzed as in Fig. 11(a). All simulation results in previous sections found the generated heat is transferred over a much larger size than the tool, so the deformation behavior of the workpiece underneath is effectively creep-dominated and elastic contributions can be neglected. Consequently, we are dealing with a circular torsional contact of a pure creeping solid in Fig. 11(a).

Our contact analysis is based on the Hill-Bower similarity relationship [46-48]. At any particular instant, the strain rates and stresses in a pure creeping solid under contact are independent of the history of loading and depend only on the instantaneous velocities and contact radius prescribed on the surface. In other words, stress and strain rate are instantaneously related with the need to recourse to history or elasticity. Any such constitutive law will work, but for clarity, it is better illustrated by a simple power law. In terms of mathematical representation, consider a power-law creeping solid with

$$\frac{\sigma}{\sigma_0} = \left(\frac{\dot{\varepsilon}}{\dot{\varepsilon}_0}\right)^{1/n}, \tag{13}$$

where σ_0 and $\dot{\varepsilon}_0$ are reference stress and reference strain rate, respectively, and n is the stress exponent as in Eq. (8). Regardless of the indenter shape (spherical, conical, or punch with a circular

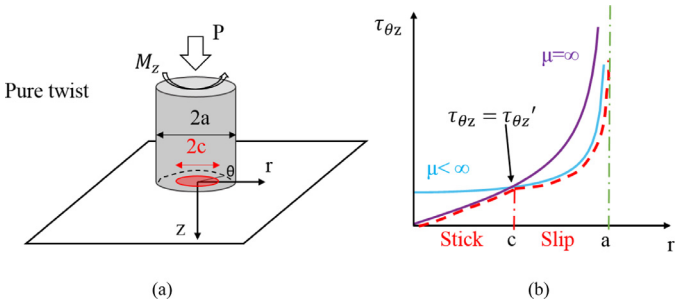

Fig. 11. (a) Schematic illustration of the stick-slip condition at the tool-workpiece interface. The boundary is circular when the lateral moving speed is much less than ωa. (b) Solutions of the interfacial shear stress.

end), the effective strain rate is given by

$$\dot{\varepsilon}_{eff} = \frac{\dot{h}}{a}, \tag{14}$$

with a being the contact radius and $\dot{h}$ being the rate of indentation depth. Therefore, the contact force P can be written as the following relationship,

$$\frac{P}{\pi a^2 \sigma_0} = \left(\frac{\dot{h}}{a\dot{\varepsilon}_0}\right)^{1/n} F_a(n, \mu_f), \tag{15}$$

with the dimensionless function F_a, and the strain rate fields are

$$\dot{\varepsilon}_{ij} = \dot{\varepsilon}_{eff} E_{ij}(x_k/a, n, \mu_f), \tag{16}$$

where E_{ij} are dimensionless functions as the characteristic fields.

Bower et al. [47] made a further step by noting the analogy between the initial value problem of a pure creeping solid under punch contact and the boundary value problem of a nonlinear elastic solid under punch contact. If replacing all the rate measures in the former by the non-rate ones (e.g., $\dot{\varepsilon}_{ij}$ by ε_{ij}), the governing equations for the former are identical to those for the latter. Therefore, the above dimensionless functions in Eqs. (15) and (16) can be numerically calculated by just finite element simulations with the nonlinear elastic law of $\sigma/\sigma_0 = (\varepsilon/\varepsilon_0)^{1/n}$.

We now use the above Hill-Bower similarity to attempt an analytical solution for our torsional contact problem in Fig. 11(a). Because the nonlinear elastic contact problem does not permit analytical solutions unless $n = 1$ (i.e., linear elastic), we make the analogy between a Newtonian viscous fluid and a linear elastic solid. The former is governed by

$$\dot{\varepsilon}_{ij} = \frac{1}{2\eta} s_{ij}, \tag{17}$$

with s_{ij} being the deviatoric stress tensor. This is merely a multiaxial generalization of Eq. (7). The latter is given by the generalized Hooke's law,

$$\varepsilon_{ij} = \frac{1+\nu}{E}\left(\sigma_{ij} - \frac{\nu}{1+\nu}\sigma_{kk}\delta_{ij}\right), \tag{18}$$

with E and ν being the Young's modulus and Poisson's ratio respectively, and δ_{ij} being the Kronecker delta. The contact solution of a Newtonian viscous material can be taken from the elastic contact solution, by replacing strain in the elastic solution by strain rate and by taking $\nu = 1/2$ due to incompressibility.

5.2. Analytical solution for the torsional contact problem

From the above subsection, it is now established that the torsional contact solution for a Newtonian viscous solid is analogous to the linear elastic problem. Due to rotational symmetry, the stick-slip boundary is circular, and the exact ratio of c/a can be derived below.

The contact pressure distribution is independent of frictional condition [49],

$$\sigma_{zz} = \frac{P}{2\pi a^2}\frac{1}{\sqrt{1-(r/a)^2}}, \tag{19}$$

so that Coulomb friction stress that sets the upper bound of interface shear stress is

$$\tau'_{\theta z} = \frac{\mu_f P}{2\pi a^2}\frac{1}{\sqrt{1-(r/a)^2}}. \tag{20}$$

For infinite friction ($\mu_f = \infty$), the shear stress distribution that generates a rotational displacement field of $u_\theta = r\theta$ is given by

$$\tau_{\theta z}|_{\mu=\infty} = \frac{3M^*}{4\pi a^3}\frac{r/a}{\sqrt{1-(r/a)^2}}, \tag{21}$$

where the torque parameter M^* remains to be determined.

As shown in Fig. 11(b), both Eqs. (20) and (21) have the same inverse square root singularity when $r \to a^-$, as the same singularity near a crack tip. The purple curve for Eq. (21) and the blue curve for Eq. (20) naturally intercepts at a location of $r = c$ by equating these two equations, so that $M^* = 2a^2\mu_f P/3c$. Taking the lower bound of these two solutions, the red dashed curve becomes the approximate solution of the shear stress,

$$\tau_{\theta z}|_{\mu<\infty} = \frac{\mu_f P}{2\pi a^2}\begin{cases} \frac{a}{c}\frac{r/a}{\sqrt{1-r/a^2}}, & r \le c: \text{ stick} \\ \frac{1}{\sqrt{1-(r/a)^2}}, & c \le r \le a: \text{ slip} \end{cases} \tag{22}$$

In other words, the twist stress needed to maintain a perfect bonding (as in infinite friction) is much larger than the upper bound value dictated by the Coulomb friction stress. Therefore, as the rotational angle increases, the slip zone emerges from the contact edge and progresses inward until the entire contacting surface is in sliding condition. Such an elastic solution mimics the stick-slip of a laterally sliding contact, in which the increase of lateral motion will lead to the emergence of annular slip zone and then the propagation towards the center of the contact corresponds to the onset of macroscopic sliding. This is well studied by the Mindlin-Cattaneo solution for Coulomb friction [49], and by some other variant solutions for different friction models [50-52].

The solution analogy between the Newtonian viscous material and the Hookean solid can now lead to the following understanding. For elastic contacts, the rotation angle dictates the degree of stick-slip ratio of c/a. Due to the analogy, the rotation angle is now replaced by its rate, i.e., the rotation speed of ω. Therefore, for our creeping solid under contact, it is ω that dictates the stick-slip behavior. In other words, given a set of processing parameters, there will be a steady state with a fixed c/a ratio.

The resulting torque on the tool can be calculated from $M_z = \int_0^a \tau_{\theta z}|_{\mu<\infty} 2\pi r dr$, which can be written as the following dimensionless function,

$$\frac{M_z}{\mu P a} = \Pi_M(c/a). \tag{23}$$

As given in Fig. 12(a), $\Pi_M(c/a)$ decreases from about 0.78 (from numerical quadrature) to 2/3 (analytical result) when c/a varies from 0 to 1.

The total heat generation rate can be computed from the above result and Eq. (6). For the simplified case of neglecting elasticity and assuming $\alpha_{TQ} = 1$, we have $Q_{total} = \omega M_z$. It should be noted that c/a depends on ω, so we need to introduce a characteristic rotation speed ω_0 for the following dimensionless function,

$$\frac{Q_{total}}{\mu P a \omega_0} = \frac{\omega}{\omega_0}\Pi_M(c/a). \tag{24}$$

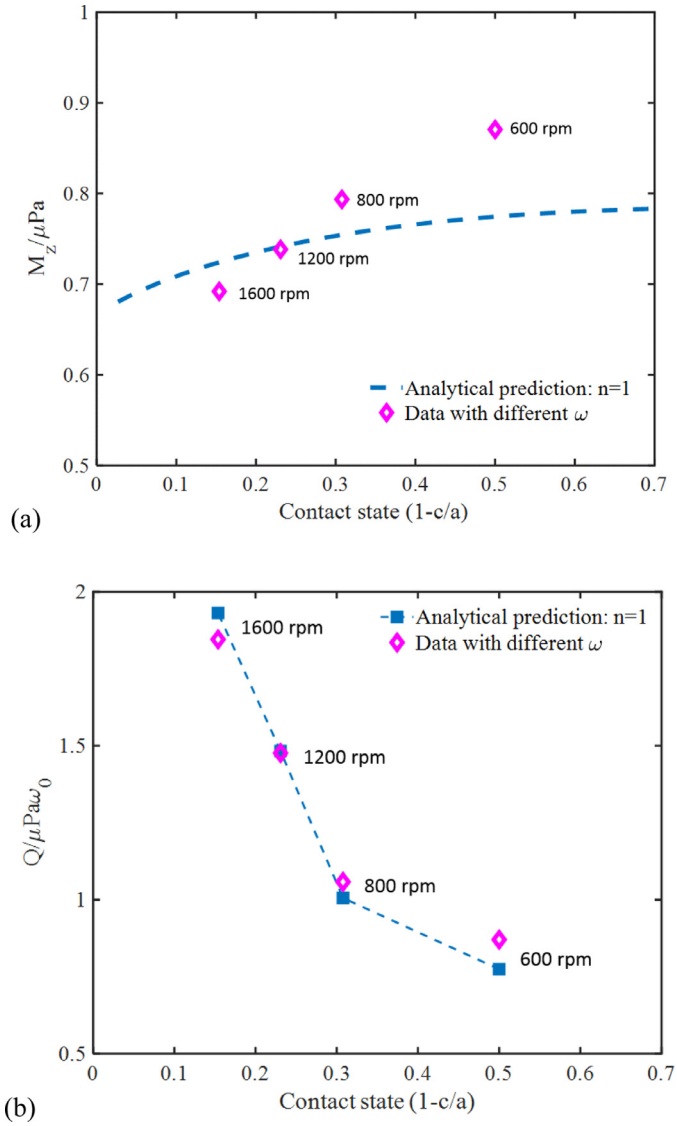

Fig. 12. Analytical prediction of the normalized torque in (a) and the normalized heat generate rate in (b) as a function of the contact state (i.e., $1-c/a$), together with the CFD simulation results based on the empirical friction boundary condition in Fig. 4(b). The parameter ω_0 is 600 rpm.

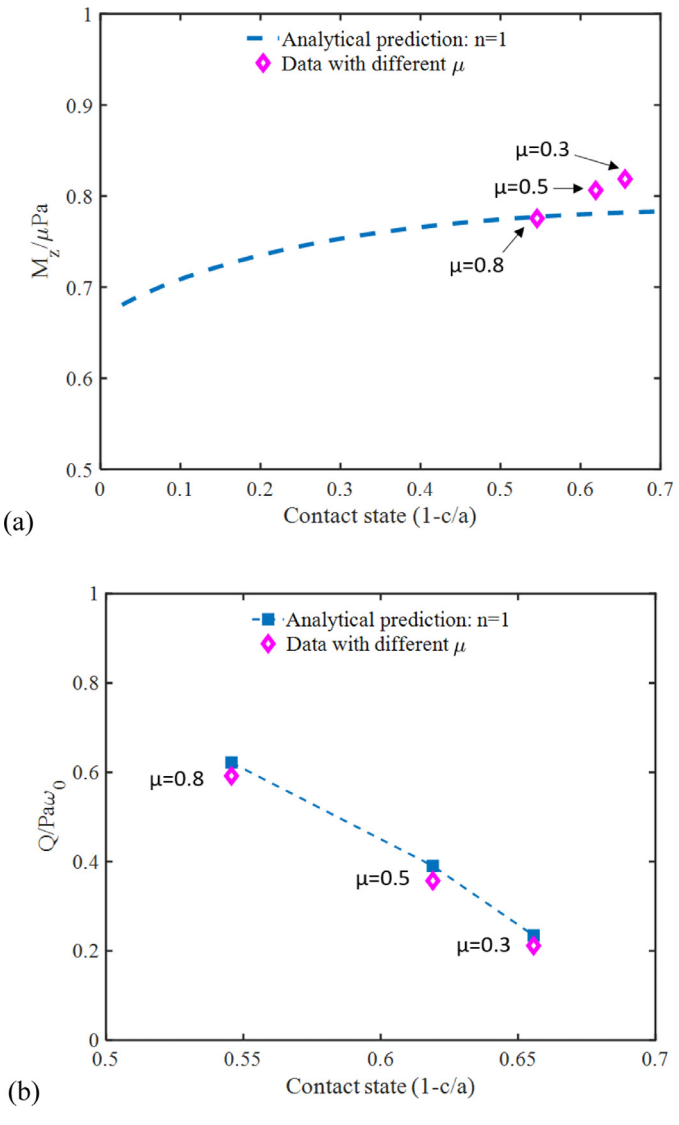

Fig. 13. Analytical prediction of the normalized torque in (a) and the normalized heat generate rate in (b) as a function of the contact state (i.e., $1-c/a$), together with the CEL simulation results that correspond to results in Figs. 7-10. The parameter ω_0 is 1000 rpm.

5.3. Comparisons to numerical simulations

As pointed out in Bower et al. [47], dimensionless functions such as F_a in Eq. (15) and E_{ij} in Eq. (16) are not so sensitive to n, unless $n \to \infty$. Therefore, it is anticipated that our approximate yet analytical solution may be used to compare to the numerical simulation results.

Comparisons to CFD simulations are presented in Fig. 12, for which we take the results by the empirical friction stress model in Figs. 3(b) and 4(b). In Fig. 12(a), the blue dashed curve represents our analytical result in Eq. (23), plotted against the contact state (i.e., $1-c/a$). The left and right ends of the abscissa thus correspond to fully stick and fully slip conditions, respectively. Data processed from CFD simulations are represented by pink rhombus markers labeled with the corresponding ω value. As shown previously in Fig. 4, increasing ω increases the stick-slip ratio of c/a, and at the same time, both numerical simulations and our analytical model show the decrease of the resulting torque in Fig. 12(a). Although the normalized torque, $M_z/\mu_f Pa$, does not vary significantly, its weak dependence on c/a is well captured here. The corresponding normalized heat generation rate is obtained through analytical solution and post-processing of CFD simulation results, as plotted in Fig. 12(b). As the pink rhombus markers show, a higher rotation speed in numerical simulations results into a larger stick-slip ratio and a higher total heat generation rate, in almost perfect agreement with the predictions by our analytical model.

Comparisons to CEL simulation results in Figs. 7-10 are presented in Fig. 13. The tool rotation speed was fixed in these simulations, but three friction coefficients were adopted. For the normalized torque in Fig. 13(a), it can be seen that the increase of friction coefficient will increase the sticking zone size (clearly $c/a \to 1$ as $\mu_f \to \infty$), and at the same time, the normalized torque decreases as the analytical solution has predicted. For the normalized total heat generation rate in Fig. 13(b), a higher friction coefficient on the contact surface will lead to a larger stick-slip ratio of c/a and a much higher total heat generation rate, again in almost perfect agreement with our analytical predictions.

The above comparisons in Figs. 12-13 suggest that the two analytical results in Eqs. (23)and (24) provide successful rational anal-

yses that relate $M_z/\mu_f Pa$ and $Q_{total}/\mu_f Pa\omega_0$ to the interfacial stick-slip ratio of c/a. CFD simulations are always based on ad hoc interface conditions (such as those in Figs. 3(a) and 3(b)), and therefore they may not predict the same c/a (and thus the same corresponding torque and heat generation rate) as CEL simulations. Nevertheless, all simulation results collapse onto the same master curves of $M_z/\mu_f Pa$~c/a and $Q_{total}/\mu_f Pa\omega_0$~$c/a$, which provides an alternative way to tuning these simulation methodologies in addition to the common practice of fitting to medium- and far-range temperature fields.

5.4. Comparisons to experimental measurements

A vast majority of experimental data have no reports on the stick-slip ratio, except for some recent breakthrough works by Shercliff and co-authors [28-30]. In these works, the material flow can be visualized by etching and showing the contrasts of two types of aluminum alloys after the friction stir spot welding. These results have motivated them to develop a kinematically determined velocity profile that resembles our results in Fig. 10. According to these empirically derived stick-slip ratio, kinematically specified contact conditions on the tool-workpiece interface were applied in numerical models to investigate the heat generation during friction stir spot welding processing. Our work here, on the other hand, suggests a systematic change of c/a significantly affects the predicted heat generation. A close comparison to Shercliff et al. [28-30] awaits further investigations.

From many other literature experiments, we can make comparisons to macroscopic thermomechanical responses, including the torque, total heat generation rate, peak temperature, and others. Peel et al. [53] have conducted extensive FSW tests on a number of aluminum alloys with a wide range of processing parameters. Their torque and axial force data are compiled and processed to generate the normalized torque values, which are then compared to our analytical model and numerical simulations in Fig. 14(a). Although their aluminum alloys are different from the AA2024 studied here, the dependence of $M_z/\mu_f Pa$ on ω/ω_0 shows the same trend, and the same range of variation, as our analytical solution and numerical data (from Fig. 12(a)).

Sato et al. [54] obtained the relationship between tool rotational speed and peak temperature in FSW process for 6000 series aluminum alloy through experiments. A rudimentary heat transfer analysis based on Rosenthal solution shows that the temperature rise, $\Delta T = T_{peak} - T_{initial}$, is proportional to $Q_{total}/2\pi ka$. The experimental finding of increasing peak temperature with the increase of rotation speed agrees with our results in Fig. 12(b). Roy et al. [55] and Nandan et al. [3] complied literature experimental data according to two dimensionless parameters, $T^* = T_p/T_{initial}$ with T_p being the final temperature, $Q^* = f\sigma_8 A_{shoulder}\omega C_P/kU^2$, where f is the heat transfer ratio between tool and workpiece, σ_8 is the yield stress, $A_{shoulder}$ is the cross-sectional area of tool shoulder, and U is the tool traveling speed. They have found a good curve fitting to the following equation,

$$T^* = 0.131 \ln Q^* + 0.196. \tag{25}$$

In Fig. 14(b), selected complied data in Roy et al. [55] are plotted, overlaid with our results of the dependence of $Q_{total}/\mu_f Pa\omega_0$ on ω/ω_0. Because of different ways of normalizing the total heat generation rate, this plot should only be understood as showing the same qualitative trend, i.e., a significant increase of the heat generation rate with the increase of tool rotation speed.

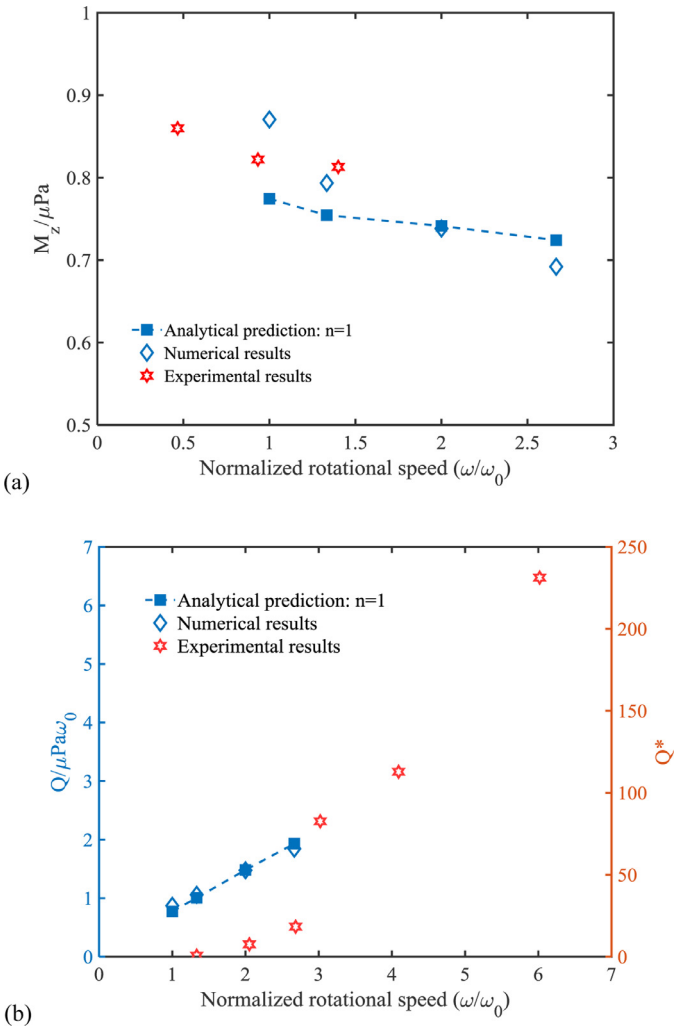

Fig. 14. Comparisons among our analytical model, numerical simulations, and literature experimental data on: (a) the normalized torque (with experimental data compiled from Peel et al. [53], and (b) the normalized total heat generation rate (with experimental data compiled from Roy et al. [55]). Numerical simulations are from Fig. 12, so that ω_0 is 600 rpm.

6. Summary

This work shows that the FSW thermomechanical responses relate to the processing, geometric, and material constitutive parameters through the interfacial stick-slip ratio of c/a. Main findings are summarized below.

(1) For CFD-based models for FSW process simulation, we have implemented the pseudo-sticking-state model in Fig. 3(a) and the empirical friction stress model in Fig. 3(b) for the interfacial condition into FLUENT. Although the stick-slip behavior can be produced in these models, their predicted c/a values are different and sensitive to their chosen parameters. Consequently, the resulting temperature and strain rate fields in workpiece materials are found to be sensitive to these ad hoc interface models, and correspondingly tedious parameter-fitting and iterative steps (particularly for avoiding predefining a uniform contact pressure) may be required for these CFD results to be predictive.

(2) CEL-based finite element simulations solve the contact problem under Coulomb friction, so that the computed thermomechanical fields are more reliable although computational cost and convergence issue are still the bottleneck concern.

(3) Based on the Hill-Bower similarity analysis for contact problem and the solution analogy between Newtonian viscous material and linear elastic solid, we have derived an approximate yet analytical solution, from which two dimensionless functions can be determined for $M_z/\mu_f Pa \sim c/a$ and $Q_{total}/\mu_f Pa\omega_0 \sim c/a$. These analytical predictions agree very well with the CFD and CEL simulations, and also align with the reported trends in some recent experiments.

(4) Our numerical and theoretical investigations of temperature and strain-rate fields provide the critical inputs for the bonding analysis. Particularly, the dimensional analysis for torque and total heat generation rate allows us to derive the dependence of bonding extent and fidelity on the processing, geometric, and material constitutive parameters, as will be detailed in our future work.

Declaration of Competing Interest

The authors declare no competing interests.

Acknowledgements

The authors would like to acknowledge the financial support of US Army Ground Vehicle Systems Center, made possible through IIP-1540000 and IIP-1822186 from the US National Science Foundation, Industry University Cooperative Research Center (I/UCRC) program, to the University of Tennessee under the Manufacturing and Materials Joining Innovation Center (Ma2JIC). The research is also supported in part from US Department of Energy, Office of Nuclear Energy's Nuclear Energy Enabling Technologies Program, through Oak Ridge National Laboratory, managed by UT-Battelle, LLC, under Contract No. DE-AC05-00OR22725 with the U.S. Department of Energy.

References

[1] R.S. Mishra, Z. Ma, Friction stir welding and processing, Mater. Sci. Eng. R 50 (2005) 1–78.
[2] K.J. Colligan, R.S. Mishra, A conceptual model for the process variables to heat generation in friction stir welding of aluminum, Scripta Mater. 58 (2008) 327–331.
[3] R. Nandan, T. DebRoy, H.K.D.H. Bhadeshia, Recent advances in friction-stir welding – process, weldment structure and properties, Prog. Mater. Sci. 53 (2008) 980–1023.
[4] D.M. Neto, P. Neto, Numerical modeling of friction stir welding process: a literature review, Int. J. Adv. Manuf. Technol. 65 (2013) 115–126.
[5] Z. Feng, R. Steel, S. Packer, S.A. David, Friction stir welding of API Grade 65 steel pipes, in: Proceedings of ASME 2009 Pressure Vessels and Piping Conference, 6, Prague, Czech Republic, 2009, pp. 775–779.
[6] Z. Yu, H. Choo, Z. Feng, S.C. Vogel, Influence of thermo-mechanical parameters on texture and tensile behavior of friction stir processed Mg alloy, Scripta Mater. 63 (2010) 1112–1115.
[7] Y.C. Lim, S. Sanderson, M. Mahoney, Y. Wang, J. Chen, S.A. David, Z. Feng, Fabrication of thick multilayered steel structure using A516 Grade 70 by multipass friction stir welding, Sci. Tech. Weld. Join. 21 (2016) 564–569.
[8] N. Switzner, Z. Yu, M. Eff, T. Lienert, A. Fonseca, Microstructure and mechanical property variations with inertia friction-welded joints of stainless steel to steel, Int. J. Adv. Manu. Tech. 95 (2018) 4327–4340.
[9] W. Cai, G. Daehn, A. Vivek, J. Li, H. Khan, R.S. Mishra, M. Komarasamy, A state-of-the-art review on solid-state metal joining, J. Manu. Sci. Eng. 141 (2019) 031012.
[10] X. Wang, Y. Gao, M. McDonnell, Z. Feng, On the solid-state-bonding mechanism in friction stir welding, Extreme Mech. Lett. 37 (2020) 100727.
[11] T. Seidel, A.P. Reynolds, Two-dimensional friction stir welding process model based on fluid mechanics, Sci. Tech. Weld. Join. 8 (2003) 175–183.
[12] P. Ulysse, Three-dimensional modeling of the friction stir-welding process, Int. J. Mach. Tools Manuf. 42 (2002) 1549–1557.
[13] P.A. Colegrove, H.R. Shercliff, Experimental and numerical analysis of aluminum alloy 7075-T7351 friction stir welds, Sci. Tech. Weld. Join. 8 (2003) 360–368.
[14] P.A. Colegrove, H.R. Shercliff, 3-Dimensional CFD modelling of flow round a threaded friction stir welding tool profile, J. Mater. Proc. Tech. 169 (2005) 320–327.
[15] H. Schmidt, J. Hattel, J. Wert, An analytical model for the heat generation in friction stir welding, Model. Simul. Mater. Sci. Eng. 12 (2003) 143–157.
[16] H. Schmidt, J. Hattel, Heat source models in simulation of heat flow in friction stir welding, Int. J. Offshore Polar Eng. 14 (2004) 296–304.
[17] Z. Yu, W. Zhang, H. Choo, Z. Feng, Transient heat and material flow modeling of friction stir processing of magnesium alloy using threaded tool, Metall. Mater. Trans. A 43 (2012) 724–737.
[18] B. Liechty, B. Webb, Modeling the frictional boundary condition in friction stir welding, Int. J. Mach. Tools Manu. 48 (2008) 1474–1485.
[19] G. Chen, Z. Feng, Y. Zhu, Q. Shi, An alternative frictional boundary condition for computational fluid dynamics simulation of friction stir welding, J. Mater. Eng. Perform. 25 (2016) 4016–4023.
[20] X. Liu, G. Chen, J. Ni, Z. Feng, Computational fluid dynamics modeling on steady-state friction stir welding of aluminum alloy 6061 to TRIP steel, J. Manu. Sci. Eng. 139 (2017) 051004.
[21] G. Chen, H. Li, G. Wang, Z. Guo, S. Zhang, Q. Dai, X. Wang, G. Zhang, Q. Shi, Effects of pin thread on the in-process material flow behavior during friction stir welding: a computational fluid dynamics study, Int. J. Mach. Tools Manuf. 124 (2018) 12–21.
[22] S. Xu, X. Deng, A.P. Reynolds, T. Seidel, Finite element simulation of material flow in friction stir welding, Sci. Tech. Weld. Join. 6 (2001) 191–193.
[23] S. Xu, X. Deng, Two and three-dimensional finite element models for the friction stir welding process, 4th Int. Symp. on Friction Stir Welding, TWI Ltd., 2003.
[24] H. Schmidt, J. Hattel, A local model for the thermomechanical conditions in friction stir welding, Model. Simul. Mater. Sci. Eng. 13 (2004) 77–93.
[25] F. Ducobu, E. Riviere-Lorphevre, E. Filippi, Application of the Coupled Eulerian-Lagrangian (CEL) method to the modeling of orthogonal cutting, Euro. J. Mech. A 59 (2016) 58–66.
[26] F. Al-Badour, N. Merah, A. Shuaib, A. Bazoune, Coupled Eulerian Lagrangian finite element modeling of friction stir welding processes, J. Mater. Proc. Tech. 213 (2013) 1433–1439.
[27] K. Chen, X. Liu, J. Ni, Thermal-mechanical modeling on friction stir spot welding of dissimilar materials based on Coupled Eulerian-Lagrangian approach, Int. J. Adv. Manuf. Technol. 91 (2017) 1697–1707.
[28] A. Reilly, H. Shercliff, Y. Chen, P. Prangnell, Modelling and visualization of material flow in friction stir spot welding, J. Mater. Proc. Tech. 225 (2015) 473–484.
[29] P. Jedrasiak, H.R. Shercliff, A. Reilly, G.J. McShane, Y.C. Chen, L. Wang, J. Robson, P. Prangnell, Thermal modeling of Al-Al and Al-steel friction stir spot welding, J. Mater. Eng. Perform. 25 (2016) 4089–4098.
[30] P. Jedrasiak, H.R. Shercliff, Small strain finite element modelling of friction stir spot welding of Al and Mg alloys, J. Mater. Proc. Tech. 263 (2019) 207–222.
[31] P.A. Colegrove, H.R. Shercliff, Development of Trivex friction stir welding tool: Part 2 – three-dimensional flow modelling, Sci. Tech. Weld. Join. 9 (2004) 352–361.
[32] P.A. Colegrove, H.R. Shercliff, CFD modelling of friction stir welding of thick plate 7449 aluminium alloy, Sci. Tech. Weld. Join. 11 (2006) 429–441.
[33] P.A. Colegrove, H.R. Shercliff, R. Zettler, A model for predicting the heat generation and temperature in friction stir welding from the material properties, Sci. Tech. Weld. Join. 12 (2007) 284–297.
[34] H. Atharifar, D. Lin, R. Kovacevic, Numerical and experimental investigations on the loads carried by the tool during friction stir welding, J. Mater. Eng. Perform. 18 (2009) 339–350.
[35] R. Nandan, G. Roy, T. Lienert, T. DebRoy, Three-dimensional heat and material flow during friction stir welding of mild steel, Acta Mater. 55 (2007) 883–895.
[36] A. Arora, R. Nandan, A.P. Reynolds, T. DebRoy, Torque, power requirement and stir zone geometry in friction stir welding through modeling and experiments, Scripta Mater. 60 (2009) 13–16.
[37] T. Sheppard, D. Wright, Determination of flow stress: Part 1 constitutive equation for aluminum alloys at elevated temperatures, Metals Tech. 6 (1979) 215–223.
[38] K.E. Tello, A.P. Gerlich, P.F. Mendez, Constants for hot deformation constitutive models for recent experimental data, Sci. Tech. Weld. Join. 15 (2010) 260–266.
[39] N. Mostaghel, T. Davis, Representations of Coulomb friction for dynamic analysis, Earthq. Eng. Struct. Dyn. 26 (1997) 541–548.
[40] M. Dirikolu, T. Childs, K. Maekawa, Finite element simulation of chip flow in metal machining, Int. J. Mech. Sci. 43 (2001) 2699–2713.
[41] G.R. Johnson, W.H. Cook, A constitutive model and data for metals subjected to large strains, high strain rates and high temperatures, in: Proceedings of the 7th International Symposium on Ballistics, The Netherlands, 1983, pp. 541–547.
[42] K.C. Mills, Recommended Values of Thermophysical Properties for Selected Commercial Alloys, Woodhead Publishing, 2002.
[43] V. Soundararajan, S. Zekovic, R. Kovacevic, Thermo-mechanical model with adaptive boundary conditions for friction stir welding of Al 6061, Int. J. Mach. Tools Manu. 45 (2005) 1577–1587.
[44] G. Chen, Q. Ma, S. Zhang, J. Wu, G. Zhang, Q. Shi, Computational fluid dynamics simulation of friction stir welding: a comparative study on different frictional boundary conditions, J. Mater. Sci. Tech. 34 (2018) 128–134.
[45] Y. Chao, S. Liu, C.H. Chien, Friction stir welding of al 6061-T6 thick plates: Part II-numerical modeling of the thermal and heat transfer phenomena, J. Chin. Inst. Eng. 3 (2008) 769–779.
[46] R. Hill, Similarity analysis of creep indentation tests, Proc. Roy. Soc. London A 436 (1992) 617–630.
[47] A.F. Bower, N.A. Fleck, A. Needleman, N. Ogbonna, Indentation of a power law creeping solid, Proc. Roy. Soc. London A 441 (1993) 97–124.

[48] J.H. Lee, Y. Gao, A.F. Bower, H.T. Xu, G.M. Pharr, Stiffness of frictional contact of dissimilar elastic solids, J. Mech. Phys. Solids 112 (2018) 318–333.
[49] K.L. Johnson, Contact Mechanics, Cambridge University Press, 1985.
[50] K.L. Johnson, Adhesion and friction between a smooth elastic spherical asperity and a plane surface, Proc. R. Soc. London A 453 (1997) 163–179.
[51] Y.F. Gao, B.N. Lucas, J.C. Hay, W.C. Oliver, G.M. Pharr, Nanoscale incipient asperity sliding and interface micro-slip assessed by the measurement of tangential contact stiffness, Scripta Mater 55 (2006) 653–656.
[52] J. Annett, Y.F. Gao, G.L.W. Cross, E.G. Herbert, B.N. Lucas, Mesoscale friction anisotropy revealed by slidingless tests, J. Mater. Res. 26 (2011) 2373–2378.
[53] M.J. Peel, A. Steuwer, P.J. Withers, T. Dickerson, Q. Shi, H. Shercliff, Dissimilar friction stir welds in AA5083-AA6082. Part I. Process parameter effects on thermal history and weld properties, Metall. Mater. Trans. A 37 (2006) 2183–2193.
[54] Y.S. Sato, M. Urata, H. Kokawa, Parameters controlling microstructure and hardness during friction-stir welding of precipitation-hardenable aluminum alloy 6063, Metall. Mater. Trans. A 33 (2002) 625–635.
[55] G. Roy, R. Nandan, T. DebRoy, Dimensionless correlation to estimate peak temperature during friction stir welding, Sci. Tech. Weld. Join. 11 (2006) 606–608.